# Design, Fabrication and Characterization of Capacitive Humidity Sensors based on Emerging Flexible Technologies

**Francisco J. Romero [1,*], Almudena Rivadeneyra [2], Alfonso Salinas-Castillo [3], Akiko Ohata [4], Diego P. Morales [1], Markus Becherer [2] and Noel Rodriguez [1]**

[1] Pervasive Electronics Advanced Research Laboratory (PEARL), Dept. Electronics and Computer Technology, University of Granada, Granada 18071, Spain; E-Mails: franromero@ugr.es; diegopm@ugr.es; noel@ugr.es
[2] Institute for nanoelectronics, Technical University of Munich, Munich, Germany; E-Mails: almudena.rivadeneyra@tum.de; markus.becherer@tum.de
[3] Dept. Analytical Chemistry, University of Granada, Granada, Spain. E-mails: alfonsos@ugr.es
[4] Institute of Space and Astronautical Science (ISAS), Japan Aerospace Exploration Agency (JAXA), Kanagawa, Japan; E-mails: ohhata.akiko@jaxa.jp
* Correspondence: franromero@ugr.es; Tel.: +34-958-248-845

**Abstract:** This work presents a case-based comparison between two emerging fabrication techniques for the development of conductive patterns for flexible electronics: inkjet-printing and nanographene production by laser-scribing. In particular, these two methods are used to fabricate planar interdigitated electrode (IDE) capacitors with Kapton® HN polyimide as supporting flexible substrate. Silver-based electrodes are manufactured by inkjet-printing, while a laser-scribing technique is used to obtain laser-reduced graphene oxide (laser-rGO) patterns from deposited graphene oxide (GO) and laser-induced graphene (LIG) layouts from the bare polyimide substrate. The comparison is focused on the application of these IDE capacitors as relative humidity (RH) sensors. The different sensors are benchmarked in terms of sensitivities to RH as well as thermal drift and linearity considering frequency dependencies. The results show that the manufactured capacitors exhibit a very competitive performance as capacitive structures when compared with other similar capacitive sensors from the literature. Furthermore, inkjet-printed and LIG-based capacitors stand out for its thermal stability and linearity.

**Keywords:** capacitive sensor; inkjet-printing; laser-induced graphene; laser-reduced graphene oxide; nanographene laser-scribing; relative humidity

## 1. Introduction

Flexible thin-film electronics is called to be one of the main actor in the more-than-moore domain, targeting auspicious applications for several areas in science and technology [1]. The rising interest in this field lies on its inherent advantages such as lightweight, flexibility and long-lasting durability, combined with cost-effective manufacturing processes [2]. Two basic approaches can be considered for the development of flexible electronics: One of them is the transfer-and-bond procedure, which consists of transferring complete circuits to flexible substrates. This technique, although intended for the development of flexible high-performance devices, requires of sophisticated fabrication processes and suffers from low scalability [3]. The other alternative is the direct production of the circuit on the flexible substrate, which bears the manufacturing of large-area electronics and yields to simpler technological processes. This approach, in turn, includes different manufacturing technologies, such as conductive inkjet-printing and nanographene laser-scribing [4-7], which are the alternatives followed in the present work.

These technologies have the advantage of being compatible with roll-to-roll techniques, enabling an inexpensive mass-production of samples. Besides, as an asset over other printing techniques, the inkjet-printing and laser-scribing processes do not precise of the use of lithographic masks or screens to define the desired layout on the substrate surface; being both *contact-less*: the process is carried out without physical contact between the nozzle (inkjet-printing) or the laser head (laser-scribing) and the substrate. Another point in favor of these technologies is the high resolution and small thickness that can be achieved when compared with other techniques such as screen printing [8]. Previous studies have already opted for these procedures to fabricate capacitive structures. Examples of them are found in the literature [9, 10], where the direct laser writing technique is used to develop graphene-based flexible supercapacitors, or the work presented by Chen et al. [11], where supercapacitors on cloth fabrics and flexible substrates are manufactured by inkjet-printing.

The present work addresses the design, fabrication and characterization of different capacitive relative humidity (RH) sensors based on interdigitated electrodes (IDEs) and manufactured by both of these methods on a commercial polyimide thin-film substrate. The same capacitive IDE structure has been defined with the different proposed techniques: One made by inkjet printing of silver nanoparticles, another one by laser-reduction of graphene oxide (laser-rGO) and the third one by laser-induction of porous graphene (LIG) directly on the substrate [12-14]. We have characterized these capacitive structures as RH sensors using a climate chamber for different environmental conditions (ranging the temperature at a fixed value of humidity and vice versa) as well as working frequencies to evaluate and compare their performance. This work is structured as follows: after this introduction, Section 2 summarizes the different materials used in our experiments as well as the methodologies followed for the fabrication and characterization of the samples. Section 3 presents the results of both structural and electrical characterization of the inkjet-printed and laser-scribed layers, together with a discussion of the capacitive sensors in terms of sensitivity to humidity, linearity, losses and thermal drift. Finally, the main conclusions are drawn in Section 4.

## 2. Materials and methods

### *2.1. Materials*

Kapton® HN films with a thickness of 125 μm were used as a flexible substrate for the implementation of the designed capacitors.

The inkjet-printed patterns were made of DGP 40LT-15C silver ink (from ANP USA Inc.) with an average content of 30% silver nanoparticles (NPs) dissolved in triethylene glycol monoethyl ether (TGME).

The graphene-oxide was obtained by in-house oxidation and sonic exfoliation of graphite powder (from Sigma-Aldrich) following a modified version of Hummers and Offerman method [15]. First, the graphite was oxidized in an ice bath with sulfuric acid ($H_2SO_4$), sodium nitrate ($NaNO_3$) and potassium permanganate ($KMnO_4$). Then, the resulting aqueous solution was filtered with hydrochloric acid (HCl) and washed ($H_2O$) to remove the remaining ions. Finally, the dispersion was sonicated in a concentration of 4 mg $mL^{-1}$ for 30 min, which causes its layer splitting [16].

### *2.2. Fabrication processes*

The inkjet-printed patterns were defined with a DMP-2831™ Dimatix printer (from Fujifilm Dimatix Inc.), which has already been used for this kind of applications [17]. The printing of the Ag ink layout over the Kapton® polyimide surface was performed under the following conditions: Drop-to-drop distance of 50 μm (being the landing diameter of 100 μm), temperature of 60 °C while printing followed, after drying, by a photonic sintering step (Sinteron 2010 from Xenon) with 5 pulses of an energy of 2.5 kV and a time lapse of 500 μs. Only one layer was needed to define the IDE structure.

The laser-scribing was performed using an in-house developed Computerized Numeric Control (CNC) driven laser diode, bypassing the use of lithographic masks. The laser head is able to modulate its power in the range from 15 to 300 mW at a fixed wavelength of 405 nm; while the engraving spatial resolution of 20 μm is given by the motors' mechanical step. Two different experimental approaches were considered for the preparation of the samples using this setup. First, the laser was used for the photothermal reduction of a graphene oxide (GO) film, prepared by drop coating on the Kapton® HN polyimide surface and dried in a vortex shaker (about 24h). Secondly, for the direct laser photothermal ablation of the Kapton® HN polyimide, which induces in its surface graphene-derived patterns with high electrical conductivity [18].

### 2.3. Capacitive sensors design

The previous fabrication processes were employed to develop planar IDE capacitive RH sensors [19-21]. The intrinsic properties of polyimides, such as its effectiveness to absorb moisture and its stability at a wide range of temperatures, make this substrate a perfect choice for the manufacturing of inexpensive RH sensors. These sensors, schematized in Figure 1.a and photographed in Figure 1.b, were designed following the IDE layout dimensions summarized in Table 1. Capacitive-type transducers offer several advantages over the resistive-type ones, such as linear humidity-capacitance relationship for a given frequency, which makes easier the definition of a calibration curve, and a wider RH range of operation [22]. The capacitance of these structures is intimately related with the relative dielectric constant ($\varepsilon_r$) of the insulators which, in the case of the Kapton® HN polyimide, increases with respect to the relative humidity (RH(%)) and decreases as the frequency ($f$) increases [23]:

$$\varepsilon_r = \boldsymbol{F}(\varepsilon_{o,r}\,,\ \mathrm{RH}(\%)\,,\ f) \tag{1}$$

being $\varepsilon_{o,r}$, dependent on the polyimide substrate. Moreover, although planar capacitors might have lower performance than parallel plate ones, the interest in planar IDE structures lies on its compactness and low thickness, which is particularly useful when the sensor is used as a conformal patch [24].

In this study, the performance of these RH sensors is evaluated as a function of the technology of the electrodes and the material between them, since they share the same flexible substrate and layout but different resolutions and thicknesses.

### 2.4. Electrodes characterization

The structural and electrical characterization of the electrodes of the capacitors are key aspects for the assessment of their performance, especially, for the laser-rGO and LIG ones. As reported by previous works, the electrical conductivity of the laser-derived graphene aggregates presents a strong dependence with the level of photothermal ablation of the raw material, which in turn depends on the power used during the scribing process [18, 25]. Therefore, the analytical structure and conductivity of the electrodes were studied as a function of the laser power with the purpose of optimizing the laser photoablation process. First, both rGO and LIG patterns were electrically characterized using the Transmission Line Model (TLM) method [26]. Once the sheet resistance of the samples was optimized as a function of the laser power, the resulting layer constituting the electrodes was structurally characterized by Scanning Electron Microcospy (SEM), Infrared (IR) spectroscopy, Raman spectroscopy, and X-ray Photoelectron Spectroscopy (XPS).

SEM images were acquired at an extraction and acceleration voltage of 5 kV using the field-emission scanning electron microscope NVision40 from Carl Zeiss. The Kratos X-ray photoelectron spectrometer model Axis Ultra-DLD were used for the XPS experiments. The samples were characterized in a vacuum chamber at a pressure $10^{-10}$ Torr using an X-ray power of 450 W. The Raman spectra acquisition was carried out in a JASCO NRS-5100 dispersive micro-Raman spectrometer with an excitation source of $\lambda$ = 532 nm (Elforlight G4-30; Nd:YAG). Finally, two different techniques were used for the IR spectroscopy, the rGO-based electrodes spectra were obtained using attenuated total reflectance Fourier transform infrared (ATR-FTIR) spectroscopy, while Diffuse Reflectance Infrared Fourier Transform (DRIFT) was used for the LIG-based electrodes since the ATR-FTIR is not sensitive enough in this case [27]. Both techniques were carried out using a Bruker Tensor 27 spectrometer.

### 2.5. Capacitive sensors characterization

The capacitance and parasitic resistance of the fabricated capacitors was measured as a function of the relative humidity and temperature using the four-wires measurement technique with the impedance analyzer 4294A and the impedance probe kit 42941A (from Keysight). The connection between the analyzer and the electrodes was done through a mini-SMA (SubMiniature version A) connector glued to each electrode using silver-filled epoxy EPO-TEK®H20E (from EpoxyTechnology, Inc.). The measurements were performed using a sinusoidal excitation signal of 0.5 V of amplitude. Furthermore, the samples were also characterized as a function of the frequency, ranging from 1 kHz to 10 MHz.

The climate chamber VCL 4006 (from VötschIndustrietechnik GmbH) was used for the characterization of the capacitive sensors under different environmental (humidity and temperature) conditions. In our experiments, the humidity was ranged between 30% and 90%, while the interval of temperature was varied from 15 °C to 65 °C.

The whole characterization setup was automatized using the Labview 2016 software (from National Instruments Corporation).

## 3. Results and discussion

### *3.1. Electrodes characterization*

The equivalent circuit of capacitors are the critical factors influencing their performance. An IDE planar capacitor can be modelled as an $R_s + R_p||C$ association, being $R_s$ the equivalent series resistance, $R_p$ the equivalent parallel resistance and $C$ its capacitance. Then, aiming to maximize the power density and to minimize the self-discharge of the capacitive structure, $R_s$ should be reduced to the minimum possible while $R_p$ should be as large as possible [28]. In our case, the series resistance is related to the sheet resistance of the electrodes, and therefore, the manufacturing processes must be optimized to minimize the resistivity of the conductive patterns.

In the case of the Ag-loaded electrodes, the sheet resistance is strongly related to the sintering method; while the conductivity of the nanographene-based ones depends on the laser photothermal power. In our experiments, we selected the photonic sintering since, as reported by a previous work [29], it can decrease the sheet resistance of the Ag ink down to 55 m$\Omega$ sq$^{-1}$ within a few milliseconds, whereas the sheet resistance of the graphene-derived patterns was studied as a function of the laser ablation level. For that purpose, the laser power was ranged from 65 mW to 100 mW at an excursion rate of 3 min cm$^{-2}$ to ensure surpassing the ablation threshold-power [30]. As observed in Figure 2, the sheet resistance of both LIG and rGO patterns presents a strong dependence with the laser power. On one hand, when the laser power is increased the sheet resistance of the rGO decreases exponentially from over-M$\Omega$ to sub-k$\Omega$. On the other hand, the LIG presents a softer decay. In both cases, the sheet resistance is reduced down to the value of ~250 $\Omega$ sq$^{-1}$. According to these results, a laser power of 100 mW was selected to minimize the resistance of both type of electrodes.

SEM images of Figure 3 show the morphology of both nanographene-derived patterns and Ag-ink layer. As seen in Figure 3a, the rGO shows a plate-shape structure with multiple cracks as a result of the photothermal reduction of the GO which indicates that the laser is able to restore, at least partially, the crystallographic structure of carbon bonds which was disrupted during the oxidation process [31]. In the case of the ablated Kapton® (Figure 3b), the irradiated regions show a foam-like morphology which is a defining feature of the LIG [13]. Besides, it can be appreciated that for the rGO sheets the reduction process supposes a thickness decrease of the original thickness of the GO film and an increase of the thickness for the LIG patterns over the Kapton® film, which is consistent with what was reported in previous works [13, 32]. It can be also seen that the engraving resolution limits the effective area of the conductive layers in both laser-treated materials. This makes the sheet resistance higher than that obtained for the Ag-ink layer since this latter, as observed in Figure 3c, is more uniform although also presents some surface porosity.

Raman spectroscopy and X-ray photoelectron spectroscopy confirm the graphene-derived nature of the rGO and LIG electrodes. On one hand, as observed in Figure 4a, the Raman spectra are dominated by three peaks: the D-peak (~1350 cm$^{-1}$), the G-peak (~1580 cm$^{-1}$) and the 2D-peak (~2700 cm$^{-1}$). These peaks are often present in disordered graphene-based materials and its ratio gives a quantification of the disorders and defects of its structure [33]. The G-peak is characteristic in sp$^2$-

hybrized carbon networks, meanwhile the D-peak comes from the structural imperfections [34]. Therefore, an estimation for the degree of disorder can be obtained from the ratio $I_D/I_G$. In this case, this ratio ($I_D/I_G \simeq 1$) points out a larger disorder in the structure of the LIG than in its rGO counterpart. The 2D-peak gives information about the number of layers of the graphite structure; its intensity increases as the number of layers decreases. Besides, there is no appreciable shift in D and 2D peaks position in both materials, while the G peak of the LIG presents a slight deviation, which might be associated to its larger number of defects [33]. In this way, according to the Raman spectroscopy results, we can infer that the LIG structure presents a lower crystallographic quality with respect to the rGO one.

On the other hand, the XPS spectrum helps to identify the remaining non-desirable bonds after the processing of the raw materials. Figure 4b shows the high resolution C1s peak of the XPS spectra for both LIG and laser-rGO electrodes. The Gaussian decomposition was resolved using the CasaXPS software (from Casa Software Ltd). As can be seen, the laser irradiation is able to break most of the C-N, C-O-C and C=O bonds which compose the Kapton® HN polyimide film and the C-OH, C=O and O=C-O bonds of the GO structure [35-37]. The resulting graphene-based materials are basically composed by carbon configurations, with prevalence of the $sp^2$ carbon aromatic rings (C-C), which is in agreement with the Raman spectroscopy results. In the case of Ag NPs patterns, XPS experiments of Figure 4c reveals the dominance of metallic silver, as confirmed by the $3d_{5/2}$ and $3d_{3/2}$ components (located at 368.1 eV and 374.1 eV, respectively) [38, 39]. These results also present a small content of carbon which remains from the TGME solvent after the drying and sintering steps, as observed in inset of Figure 4c.

IR spectroscopy also supports these results, Figure 5a shows how the reduction process of the GO significantly reduces the stretching vibrations of the hydroxyl groups (-OH) and water molecules presented in the range 3700–2800 $cm^{-1}$ as well as at ~1614 $cm^{-1}$ and 1347 $cm^{-1}$. Besides, the broad peak in the range 966–1090 $cm^{-1}$ presented in the GO due to the epoxy groups (C-O-C) is also significantly reduced, while the peak at 1580 $cm^{-1}$ indicates that the C=C band was restored [40-42]. As seen, the laser is able to remove various oxygen containing functional groups, although some carbonyl and epoxy groups (C-O-C) still remain after the reduction process. In the case of the Kapton® polyimide (Figure 5b), the aromatic C-H stretching modes, the imide C-N groups as well as the phenyl ether linkages (C-O-C) which compose its chemical structure present a significant reduction, whereas the change in the intensity of peaks at 1500 $cm^{-1}$ and 1600 $cm^{-1}$ reveals an increase in the aromaticity of the irradiated surface [43].

The resolution of the printing and scribing processes is also an important aspect for the performance of the capacitors [20, 21]. Therefore, we analyzed the real physical dimensions of the printed and laser-scribed electrodes under the microscope (see Figure 1b) to establish a comparison between the designed layout (Table 1) and the experimental one. Table 2 presents the resolution achieved by both methods, where uncertainties were calculated as the standard deviation of the experimental data. As seen, inkjet patterns have better precision (for the experimental setup considered), especially for the smallest features. Moreover, as can be seen in Figure 1b, the inkjet-printed electrodes are more uniform than the obtained by laser-scribing, which present an appreciable outline pattern because of the laser-CNC mechanical steps.

### *3.2. Capacitive sensors characterization*

Once the electrodes have been structurally and electrically characterized, hereinafter a characterization of the sensors capacitance as a function of the RH(%) and working frequency is presented. The capacitance and equivalent parallel resistance of the capacitors depicted in Figure 1 was measured for different values of RH(%) as a function of the frequency and at a constant temperature of 40 °C to be able to cover a broad range of RH . As expected, in all cases the capacitance decreases as the frequency increases. For the LIG electrodes (Figure 6a), the capacitance decays half its value, from about 8.5 pF at 1 kHz down to 4 pF at 10 MHz, whereas the response of the Ag-based electrodes (Figure 6c) shows a lower dependency on the working frequency with a mean value of 5 pF in the whole range of frequencies analyzed. These values are consequent with the different theoretical models of a coplanar IDE capacitor, such as the proposed by Qin *et al.* [44]. Moreover, for the rGO-based capacitors (Figure 6b), the capacitance at 1 kHz is about 40 pF with an exponential decay in frequency down to 5 pF at 10 MHz. As seen, the rGO capacitors present a much higher capacitance at low frequencies due to the high dielectric constant of the GO which remains between the coplanar IDE structure (as can be observed in Figure 1b). However, the capacitance reaches a similar value to the previous ones at high frequencies since the dielectric constant of the GO decreases abruptly when the frequency is increased [45].

The calibration curves of each sensor for an excitation source with a frequency of 1 kHz, 10 kHz and 100 kHz are represented in Figure 7. The study was also carried out for different frequencies due to the interest in fast readout sensors [46, 47]. The sensitivity of the sensor, *S*, which can be obtained from Eq. 2, gives information about its behavior to humidity changes [48]. Paired in importance, the linearity of the response is defined as the maximum deviation from its linear approximation (Eq. 3) [49]. Also, the hysteresis is calculated from Eq. 4, as the maximum difference of capacitance while performing the characterization by increasing and decreasing RH cyclically.

$$S = \left|\frac{\Delta C}{\Delta RH_i(\%)}\right|_{T=cte} \tag{2}$$

$$Nonlinearity = \frac{max(C_i - C_{lf})}{C_{max}} \tag{3}$$

$$Hysteresis = \frac{max(C_{i,increasing} - C_{i,decreasing})}{C_i} \tag{4}$$

being $C_i$ the experimental capacitance measured at $RH_i(\%)$, $C_{lf}$ its linear approximation and $C_{max}$ the maximum capacitance. $C_{i,increasing}$ and $C_{i,decreasing}$ are the measured capacitance at $RH_i(\%)$ while increasing and decreasing steps of RH, respectively.

The thermal drift is obtained as the sensitivity of the developed sensor to temperature changes, considering the range from 15 °C to 65 °C ($\Delta T$) at a constant relative humidity of 50%RH, see Eq. 5.

$$Thermal\ drift = \left|\frac{\Delta C}{\Delta T}\right|_{RH=cte} \tag{5}$$

A benchmarking of the parameters described above, corresponding to our transducers, is summarized in Table 3. These results are the average of several measurements carried out on different days presenting negligible changes from day to day. As can be observed, the LIG-based capacitors present higher linearity and thermal stability at the expense of a lower sensitivity. This sensitivity, which ranges from 2.0 fF/%RH to 7.44 fF/%RH as a function of the frequency, is comparable to the obtained in previous works. For example, Molina-Lopez *et al.* reported a sensitivity of 2.3 fF/%RH with an IDE structure using cellulose acetate butyrate (CAB) as sensing layer and Ag/Ni as electrode material [20], a similar structure with poly(ether urethane) (PEUT) as sensing layer and a sensitivity of 2.03 fF/%RH at 100 kHz was proposed by Altenberend *et al.* [50]. In the same way, comparable sensitivities can be found in the literature for sensors based on more complex technologies [51-53]. Besides, as it has been already demonstrated in other works, the sensitivity of these capacitive sensors might be improved using different geometrical layouts [54].

Moreover, the inkjet-printed ones present a sensitivity up to 5 times higher than LIG-based capacitors at low frequencies, however, the sensitivity decays with the frequency while their linearity and thermal drift increase. In the case of the rGO-based electrodes, the GO layer between them makes these sensors the most sensitive, although the calibration curve fits better to a second order function. These capacitors also suffer from a low thermal stability since, as it is well known, the GO is also an outstanding thermal conductor [55]. In any case, the modelling of these calibration curves results easier than the ones from the resistive-type IDE structures, that follow logarithmic or exponential functions [56, 57].

Furthermore, the equivalent parallel resistance of each capacitor is plotted as a function of the frequency in Figure 8. The change in the parallel resistance with respect to the frequency is due to the leakage current between the electrodes as a result of the dielectric losses when the frequency increases [57]. Because of it, the self-discharge resistance decreases with respect to the frequency in all cases. The best performance in terms of resistivity for the whole range of frequency is achieved by the inkjet-printed capacitors followed by the LIG ones, whose higher leakage current could be directly related to the less uniformity of its electrodes. The laser-rGO-based capacitors are the worst structures in this context since the remaining GO layer between the electrodes facilitates the flow of the leakage current. In any case, these results are very competitive when we compare them with the obtained for other very similar capacitive structures from the literature, such as the presented by Li *et al.* [58], where $R_p$ ranges from ~10 MΩ (at 1 kHz) to ~0.1 MΩ (at 100 kHz). These differences in the parallel resistance are also related to the different capacitance values illustrated in Figure 6. It can be noted that the higher the losses are (lower $R_p$), the higher the measured capacitance is.

Regarding to the fabrication technologies, inkjet-printing provides the lower value of capacitance, but better performance as capacitive structure (higher $R_p$, less losses). Besides, this performance is even better for smaller sizes, as it has been already demonstrated [21, 54]. However, this process is more expensive, non-environmentally friendly and slower than the LIG one since it requires of a sintering step. Moreover, the LIG is the simplest method since it can be carried out directly over the substrate without requiring other material or any extra fabrication steps (no previous depositions or sintering processes needed). Thus, this technology allows to obtain humidity sensors with a sensitivity comparable to the reported in the literature combining a high linearity with a low thermal drift. Besides, the performance of these sensors would be enhanced using a higher resolution engraving, which would make the LIG layer more uniform, reducing the leakage current (losses), increasing the effective area and, therefore, their sensitivity. Finally, the laser-rGO based capacitors provide much higher capacitance values from the same layout and more sensitivity. Nevertheless, these ones also present the highest losses (lowest $R_p$ values), non-linearity and thermal drift so a rGO-based solution does not result the best choice as capacitive humidity sensors. In fact, this technology is usually better suited for the development of resistive thermistors [25, 59].

Summarizing, the main difference between the graphene-based capacitors and the Ag-ink ones lies on the sheet resistance and uniformity of the conductive layer. Besides, the rGO-based sensor presents the singularity of having a remaining layer of unreduced GO in-between its electrodes. On one hand, this latter feature makes the rGO-based capacitors much more sensitive than both LIG and Ag-ink ones, since the GO dielectric constant is very sensitive to humidity and temperature changes (in contrast to air). Therefore, this also makes the rGO-based sensor thermally less stable and facilitates the current leakage between electrodes. On the other hand, the LIG electrode is less uniform and less conductive that the Ag-ink one, which increase the losses and make these sensors less sensitive.

Finally, as an example of how fast the developed sensors are, the dynamic response of the Ag-based capacitor is depicted in Figure 9. It can be note that our flexible humidity sensor presents a higher response time (~3.5 times slower) than the widely-used rigid sensor SHT31 (from Sensirion AG). Besides, this time is intimately related to the sheet resistance of the conductive patterns, being greater as the sheet resistance increases [60], and to the thickness of the sensitive layer [61].

## 5. Conclusions

Flexible planar IDE capacitive humidity sensors have been compared as a function of the materials and techniques used for its fabrication. Inkjet-printing and laser-scribing techniques have been used to fabricate three different capacitors (Ag-ink, laser-rGO and LIG) over a Kapton® polyimide substrate with the same IDE layout. The structures have been characterized in terms of RH sensitivity, linearity, thermal drift, losses and frequency response. The results obtained have demonstrated that the LIG-based capacitors present a higher linearity response to humidity changes (0.5% of non-linearity at 10 kHz) and the best thermal stability (3.26 fF/°C at 10 kHz) with a sensitivity (ranging from 2 fF/%RH to 7.44 fF/%RH) very competitive when compared with other similar sensor from the literature. On the contrary, the laser-rGO and inkjet-printing based capacitors are much more sensitive to humidity changes (up to 100 and 5 times higher, respectively), keeping a competitive value of sensitivity when the frequency is increased but presenting a higher thermal drift. The inkjet-printed capacitors also stand out for their low losses and the possibility of operating at higher frequencies, while the thermal drift and a higher non-linearity coefficient of the rGO capacitors are their main disadvantages in comparison to the other two structures studied.

**Acknowledgments**

This research was funded by the Spanish Ministry of Education, Culture and Sport (MECD), the European Union and the University of Granada through the project TEC2017-89955-P, the pre-doctoral grant FPU16/01451, the fellowship H2020-MSCA-IF-2017 794885-SELFSENS and the grant "Initiation to Research". The authors would like to thank the support of the JSPS KAKENHI through the grant number JP18K04275 and the support of the Institute for Cognitive Systems from the Technical University of Munich for the use of the inkjet printer.

# References


1. A. Nathan et al., Flexible Electronics: The Next Ubiquitous Platform, Proceedings of the IEEE 100 (2012) 1486-1517. DOI: 10.1109/JPROC.2012.2190168.
2. W. Zeng, L. Shu, Q. Li, S. Chen, F. Wang, X. Tao, Fiber-Based Wearable Electronics: A Review of Materials, Fabrication, Devices, and Applications, Adv. Mater. 26 (2014) 5310-5336. DOI: 10.1002/adma.201400633.
3. C.I. Cheng, S. Wagner, Overview of Flexible Electronics Technology, in: Flexible Electronics, W.S. Wong, A. Salleo (Eds.), Springer, Boston, MA, 2009, Volume 11, pp. 1-28. ISBN: 978-0-387-74363-9.
4. G. Cummins; M.P.Y. Desmulliez, Inkjet printing of conductive materials: a review, Circuit World 38 (2012) 193-213. DOI: 10.1108/03056121211280413.
5. B. de Gans, P. Duineveld, U. Schubert, Inkjet Printing of Polymers: State of the Art and Future Developments, Adv. Mater. 16 (2004) 203-213. DOI: 10.1002/adma.200300385.
6. M.F. El-Kady, V. Strong, S. Dubin, R.B. Kaner, Laser Scribing of High-Performance and Flexible Graphene-Based Electrochemical Capacitors, Science 335 (2012) 1326-1330. DOI: 10.1126/science.1216744.
7. J. B. In, B. Hsia, J.H. Yoo, S. Hyun, C. Carraro, R. Maboudian, C. P. Grigoropoulos, Facile fabrication of flexible all solid-state micro-supercapacitor by direct laser writing of porous carbon in polyimide, Carbon 83 (2015) 144-151. DOI: 10.1016/j.carbon.2014.11.017.
8. R. Søndergaard, M. Hösel, D. Angmo, T.T. Larsen-Olsen, F.C. Krebs, Roll-to-roll fabrication of polymer solar cells, Materials Today 15 (2012) 36-49. DOI: 10.1016/S1369-7021(12)70019-6.
9. Z. Peng, J. Lin, R. Ye, E. Samuel, J.M. Tour, Flexible and Stackable Laser-Induced Graphene Supercapacitors, ACS Appl. Mater. Interfaces 7 (2015) 3414–3419. DOI: 10.1021/am509065d.
10. W. Gao, N. Singh, L. Song, Z. Liu, A.L.M. Reddy, L. Ci, R. Vajtai, Q. Zhang, B. Wei, P.M. Ajayan, Direct laser writing of micro-supercapacitors on hydrated graphite oxide films, Nature Nanotechnology 6 (2011) 496–500. DOI:10.1038/nnano.2011.110.
11. P. Chen, H. Chen, J. Qiu, C. Zhou, Inkjet Printing of Single-Walled Carbon Nanotube/RuO2 Nanowire Supercapacitors on Cloth Fabrics and Flexible Substrates, Nano Res 3 (2010) 594-603. DOI 10.1007/s12274-010-0020-x.
12. R. Ye, D.K. James, J.M. Tour. Laser-Induced Graphene, Accounts of Chemical Research (2018). DOI: 10.1021/acs.accounts.8b00084.
13. J. Lin, Z. Peng, Y. Liu, F. Ruiz-Zepeda, R. Ye, E.L.G. Samuel, M.J. Yacaman, B.I. Yakobson, J.M. Tour, Laser-induced porous graphene films from commercial polymers, Nature Communications 5 (2014) 1-8. DOI: 10.1038/ncomms6714.
14. A. Lamberti, F. Perrucci, M. Caprioli, M. Serrapede, M. Fontana, S. Bianco, S: Ferrero, E. Tresso, New insights on laser-induced graphene electrodes for flexible supercapacitors: tunable morphology and physical properties, Nanotechnology 28 (2017) 1-9. DOI: 10.1088/1361-6528/aa6615.
15. W.S. Hummers Jr., R.E. Offeman, Preparation of Graphitic Oxide, J. Am. Chem. Soc. 80 (1958) 1339–1339. DOI: 10.1021/ja01539a017.
16. A.M. Dimiev, S. Eigler, Graphene Oxide: Fundamentals and Applications, John Wiley & Sons (Ed.), USA, 2016. ISBN: 978-1-119-06940-9.
17. A. Falco, J.F. Salmerón, F.C. Loghin, P. Lugli, A. Rivadeneyra, Fully Printed Flexible Single-Chip RFID Tag with Light Detection Capabilities, Sensors 17 (2017) 534. DOI: 10.3390/s17030534.
18. F.J. Romero, A. Salinas-Castillo, A. Rivadeneyra, A. Albrecht, A. Godoy, D.P. Morales, N. Rodriguez. In-Depth Study of Laser Diode Ablation of Kapton Polyimide for Flexible Conductive Substrates, Nanomaterials 8 (2018). DOI: 10.3390/nano8070517.
19. T. Yang, Y.Z. Yu, L.S. Zhu, X. Wu, X.H. Wang, J. Zhang, Fabrication of silver interdigitated electrodes on polyimide films via surface modification and ion-exchange technique and its flexible humidity sensor application, Sens Actuators B Chem 208 (2015) 327-333. DOI: 10.1016/j.snb.2014.11.043.

20. F. Molina-Lopez, D. Briand, N.F. de Rooij, All additive inkjet printed humidity sensors on plastic substrate, Sens Actuators B Chem, 166 (2012), 212-222. DOI: 10.1016/j.snb.2012.02.042.
21. A. Rivadeneyra, J. Fernández-Salmerón, M. Agudo, J.A. López-Villanueva, L.F. Capitan-Vallvey, A.J. Palma, Design and characterization of a low thermal drift capacitive humidity sensor by inkjet-printing, Sens Actuators B Chem, 195 (2014) 123-131. DOI: 10.1016/j.snb.2013.12.117.
22. P.M. Harrey, B.J. Ramsey, P.S.A. Evans, D.J. Harrison, Capacitive-type humidity sensors fabricated using the offset lithographic printing process, Sens Actuators B Chem 87 (2002) 226-232. DOI: 10.1016/S0925-4005(02)00240-X.
23. DUPONT™ KAPTON®: Summary of Properties [Accessed on 15 October 2018].
24. S. Amendola, R. Lodato, S. Manzari, C. Occhiuzzi, G. Marrocco, RFID Technology for IoT-Based Personal Healthcare in Smart Spaces, IEEE Internet of Things Journal 1 (2014) 144-152. DOI: 10.1109/JIOT.2014.2313981.
25. F.J. Romero, A. Rivadeneyra, V. Toral, E. Castillo, F. García-Ruiz, D.P. Morales, N. Rodriguez, Design guidelines of laser reduced graphene oxide conformal thermistor for IoT applications, Sensors and Actuators A: Physical 274 (2018) 148-154. DOI: 10.1016/j.sna.2018.03.014.
26. G.K. Reeves, H.B. Harrison, Obtaining the specific contact resistance from transmission line model measurements, IEEE Electron Device Letters 3 (1982) 111-113. DOI: 10.1109/EDL.1982.25502.
27. E.E. Ortelli, F. Geiger, T. Lippert, J. Wei, A. Wokaun, UV-Laser-Induced Decomposition of Kapton Studied by Infrared Spectroscopy, Macromolecules 33 (2000) 5090–5097. DOI: 10.1021/ma000389a.
28. E. Frackowiak, F. Beguin, Carbon materials for the electrochemical storage of energy in capacitors, Carbon 39 (2001) 937-950. DOI: 10.1016/S0008-6223(00)00183-4.
29. A. Albrecht, A. Rivadeneyra, A. Abdellah, P. Lugli, J.F. Salmeron, Inkjet printing and photonic sintering of silver and copper oxide nanoparticles for ultra-low-cost conductive patterns, J. Mater. Chem. C 4 (2016) 3546-3554. DOI: 10.1039/c6tc00628k.
30. S. Küper, J. Brannon, K. Brannon, Threshold behavior in polyimide photoablation: Single-shot rate measurements and surface-temperature modeling, Applied Physics A 56 (1993) 43-50. DOI: 10.1007/BF00351902.
31. E.P. Neustroev, M.V. Nogovitsyna, Y.S. Solovyova, G.N. Alexandrov, E.K. Burtseva, Study of Electrical Conductivity of Thermally Reduced Graphene Oxide, RENSIT Nanosyst. 7 (2015) 162–167. DOI: 10.17725/rensit.2015.07.162.
32. Z. Wan, S. Wang, B. Haylock, J. Kaur, P. Tanner, D. Thiel, R. Sang, I.S. Cole, X. Li, M. Lobino, Q. Li, Tuning the sub-processes in laser reduction of graphene oxide by adjusting the power and scanning speed of laser, Carbon 141 (2019) 83–91. DOI: 10.1016/j.carbon.2018.09.030.
33. J.B. Wu, M.L. Lin, X. Cong, H.N. Liu, P.H. Tan, Raman spectroscopy of graphene-based materials and its applications in related devices, Chemical Society Reviews 47 (2018) 1822. DOI: 10.1039/C6CS00915H.
34. S. Venkatachalam, D. Bertin, G. Ducournau, J.F. Lampin, D. Hourlier, Kapton-derived carbon as efficient terahertz absorbers, Carbon 100 (2016) 158-164. DOI: 10.1016/j.carbon.2016.01.003.
35. K.C. Yung, D.W. Zeng, T.M. Yuem, XPS investigation of Upilex-S polyimide ablated by 355 nm Nd:YAG laser irradiation, Applied Surface Science 173 (2001) 193-202. DOI: 10.1016/S0169-4332(00)00884-9.
36. C.Z. Hu, L. Feng, J.D. Andrade, Surface structure of pyrolyzed polyimide, Carbon 26 (1988) 543-545. DOI: 10.1016/0008-6223(88)90153-4.
37. S. Yumitori, Correlation of C1s chemical state intensities with the O1s intensity in the XPS analysis of anodically oxidized glass-like carbon samples, Journal of Materials Science 35 (2000) 139-146. DOI: 10.1023/A:1004761103919.
38. X. Xu, J. Zhuang, Y. Du, H. Feng, N. Zhang, C. Liu, T. Lei, J. Wang, M. Spencer, T. Morishita, X. Wang, S.X. Dou, Effects of Oxygen Adsorption on the Surface State of Epitaxial Silicene on Ag(111), Scientific Reports 4 (2014), 7543. DOI: 10.1038/srep07543.

39. J. Jayabharathi, G.A. Sundari, V. Thanikachalam, P. Jeeva, S. Panimozhi, A dodecanethiol-functionalized Ag nanoparticle-modified ITO anode for efficient performance of organic light-emitting devices, RSC Adv 7 (2017) 38923-38934. DOI: 10.1039/C7RA07080B.
40. J.V. Piovesan, E.R. Santana, A. Spinelli, Reduced graphene oxide/gold nanoparticles nanocomposite-modified glassy carbon electrode for determination of endocrine disruptor methylparaben, J. Electroanal. Chem 813 (2018) 163-170. DOI: 10.1016/j.jelechem.2018.02.025.
41. M. Ciszewski, A. Mianowski, P. Szatkowski, G. Nawrat, J. Adamek, Reduced graphene oxide–bismuth oxide composite as electrode material for supercapacitors, Ionics 21 (2015) 557-563.
42. B.A. Aragaw, W.N. Su, J. Rick, B.J. Hwang, Highly efficient synthesis of reduced graphene oxide–Nafion nanocomposites with strong coupling for enhanced proton and electron conduction, RSC Adv. 3 (2013) 23212–23221.
43. J.E. Ferl, E.R. Long, Infrared Spectroscopic Analysis of the Effects of Simulated Space Radiation on a Polyimide, IEEE Trans Nucl Sci 28 (1981) 4119 – 4124. DOI: 10.1109/TNS.1981.4335686.
44. H. Qin, Y. Cai, J. Dong and Y.S. Lee, Direct Printing of Capacitive Touch Sensors on Flexible Substrates by Additive E-Jet Printing With Silver, J. Manuf. Sci. Eng. 139 (2017) 031011. DOI: 10.1115/1.4034663.
45. K.S. Kumar, S. Pittala, S. Sanyadanam, P. Paik, A new single/few-layered graphene oxide with a high dielectric constant of 106 contribution of defects and functional groups, RSC Adv. 5 (2015) 14768. DOI: 10.1039/c4ra10800k.
46. X. Zhang, M. Liu, B. Wang, H. Chen, Z. Wang, A Wide Measurement Range and Fast Update Rate Integrated Interface for Capacitive Sensors Array, IEEE Transactions on Circuits and Systems I: Regular Papers 61 (2014) 2-11. DOI: 10.1109/TCSI.2013.2264696.
47. A. Gaißer, W. Geiger, T. Link, J. Merz, S. Steigmajer, A. Hauser, H. Sandmaiera, W. Lang, N. Niklasch, New digital readout electronics for capacitive sensors by the example of micro-machined gyroscopes, Sensors and Actuators A: Physical 97-98 (2002) 557-562. DOI: 10.1016/S0924-4247(02)00045-6.
48. Y. Wang, S. Parka, J.T.W. Yeow, A. Langner, F. Müller, A capacitive humidity sensor based on ordered macroporous silicon with thin film surface coating, Sens Actuators B Chem 149 (2010) 136-142. DOI: 10.1016/j.snb.2010.06.010.
49. Y. Kim, B. Jung, H. Lee, H. Kim, K. Lee, H. Park, Capacitive humidity sensor design based on anodic aluminum oxide, Sens Actuators B Chem 141 (2009) 441-446. DOI: 10.1016/j.snb.2009.07.007.
50. U. Altenberend, F. Molina-Lopez A. Oprea, D. Briand, N. Bârsan, N.F. De Rooij, U. Weimar, Towards fully printed capacitive gas sensors on flexible PET substrates based on Ag interdigitated transducers with increased stability, Sens Actuators B Chem 187 (2013) 280-287. DOI: 10.1016/j.snb.2012.11.025.
51. A. Vásquez-Quintero, N. Frolet, D. Märki, A. Marette, G. Mattana, D. Briand, N.F. De Rooij, 2014 IEEE 27th International Conference on Micro Electro Mechanical Systems (MEMS). DOI: 10.1109/MEMSYS.2014.6765695.
52. A. Rivadeneyra, J.F. Salmeron, L.F. Capitan-Vallvey, A.J. Palma, Characterization of an Interdigitated Capacitive Structure With Branches for Relative Humidity Sensing, IEEE Sensors Letters 1 (2017) 1500404. DOI: 10.1109/LSENS.2017.2737080.
53. G. Mattana, T. Kinkeldei, D. Leuenberger, C. Ataman, J.J. Ruan, F. Molina-Lopez, A. Vásquez-Quintero, G. Nisato, G. Tröster, D. Briand, N.F. De Rooij, Woven Temperature and Humidity Sensors on Flexible Plastic Substrates for E-Textile Applications, IEEE Sensors Journal 13 (2013) 3901 – 3909. DOI: 10.1109/JSEN.2013.2257167.
54. A. Rivadeneyra, J. Fernández-Salmeron, M. Agudo-Acemel, J.A. López-Villanueva, L.F. Capitan-Vallvey, A.J. Palma, Printed electrodes structures as capacitive humidity sensors: A comparison, Sensors and Actuators A: Physical 244 (2016) 56-65. DOI: 1 0.1016/j.sna.2016.03.023.
55. Y. Zhu, S. Murali, W. Cai, X. Li, J.W. Suk, J.R. Potts, R.S. Ruoff, Graphene and Graphene Oxide: Synthesis, Properties, and Applications, Adv. Mater. 22 (2010) 3906-3924. DOI: 10.1002/adma.201001068.

56. P.G. Su, C.C. Shiu, Electrical and sensing properties of a flexible humidity sensor made of polyamidoamine dendrimer-Au nanoparticles, Sens Actuators B Chem 165 (2012) 151–156. DOI: 10.1016/j.snb.2012.02.032.
57. V. Ruiz, I. Fernández, P. Carrasco, G. Cabanero, H.J. Grande, J. Herrán, Graphene quantum dots as a novel sensing material for low-cost resistive and fast-response humidity sensors, Sens Actuators B Chem 218 (2015) 73–77. DOI: 10.1016/j.snb.2015.04.092.
58. Y. Li, R. Torah, S. Beeby, J. Tudor, An all-inkjet printed flexible capacitor on a textile using a new poly (4-vinylphenol) dielectric ink for wearable applications, IEEE Sensors (2012). DOI: 10.1109/ICSENS.2012.6411117.
59. B. Davaji, H. D. Cho, M. Malakoutian, J.K. Lee, G. Panin, T.W. Kang, C.H. Lee, A patterned single layer graphene resistance temperature sensor, Scientific Reports 7 (2017) 8811. DOI: 10.1038/s41598-017-08967-y.
60. A. Oprea, N. Bârsan, U. Weimar, M.L. Bauersfeld, D. Ebling, J. Wöllenstein. Capacitive humidity sensors on flexible RFID labels, Sensors and Actuators B: Chemical 132 (2008). DOI: 10.1016/j.snb.2007.10.010.
61. S. Borini, R. White, D. Wei, M. Astley, S. Haque, E. Spigone, N. Harris, J. Kivioja, T. Ryhänen. Ultrafast Graphene Oxide Humidity Sensors, ACS Nano 7 (2013). DOI: 10.1021/nn404889b.

# Figures and Tables

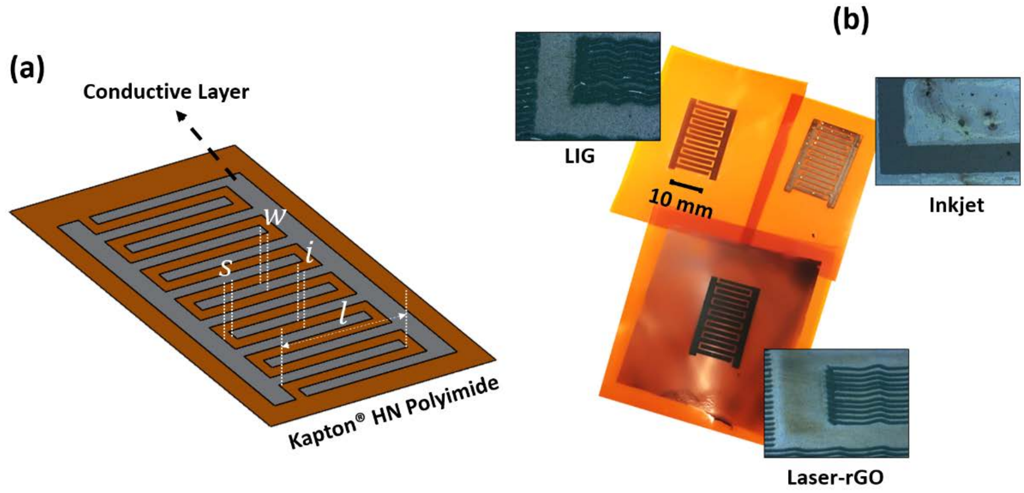


Figure 1. (a) Planar IDE capacitor on Kapton® HN polyimide substrate (w: finger width; s: electrode separation; i: finger interspacing; l: finger length). (b) Actual photographs and microscope images of an Ag-ink printed electrode, a laser-induced graphene electrode and a laser-rGO electrode.

**Table 1.** Planar IDE capacitors layout description.

| Parameter | Value |
|---|---|
| Number of fingers | 13 |
| Fingers length (*l*) | 10 mm |
| Fingers width (*w*) | 1 mm |
| Fingers interspacing (*i*) | 0.5 mm |
| Electrodes separation (*s*) | 0.5 mm |

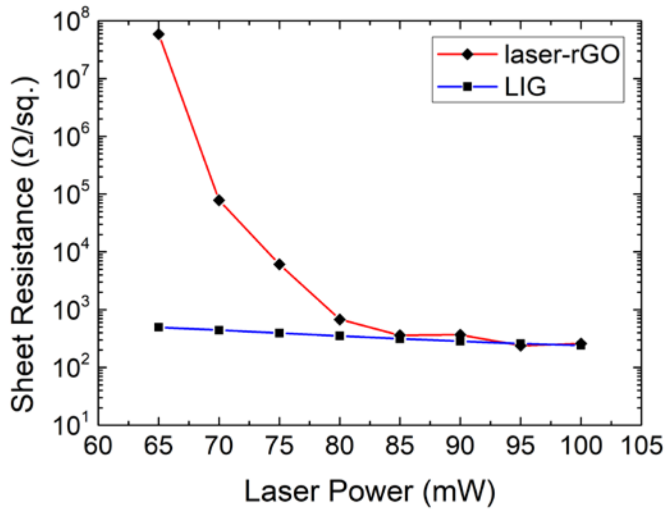


**Figure 2.** Sheet resistance of the LIG and laser-rGO as a function of the laser power used for the photoablation of the polyimide surface and the graphene oxide reduction respectively. The laser excursion rate was set to 3 min $cm^{-2}$.

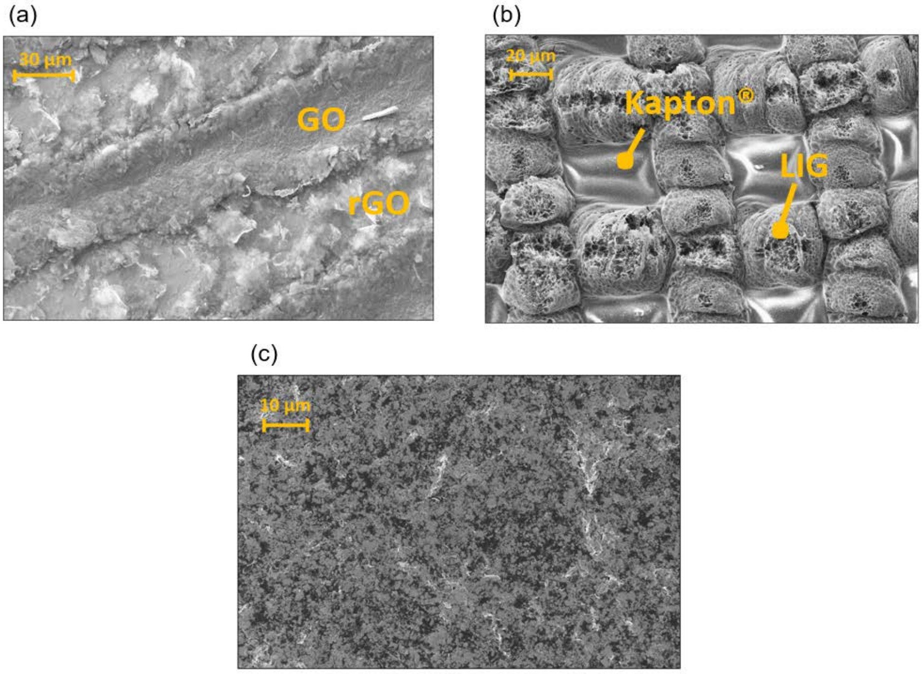


**Figure 3.** (a) SEM image of a laser-reduced GO sample (scale: 30 µm, extraction and acceleration voltage: 5 kV, working distance: 6.0 mm). (b) SEM image of a laser-ablated Kapton® sample (scale: 20 µm, extraction and acceleration voltage: 5 kV, working distance: 6.0 mm). (c) SEM image of an Ag-ink sample (scale: 10 µm, extraction and acceleration voltage: 5 kV, working distance 6.0 mm).

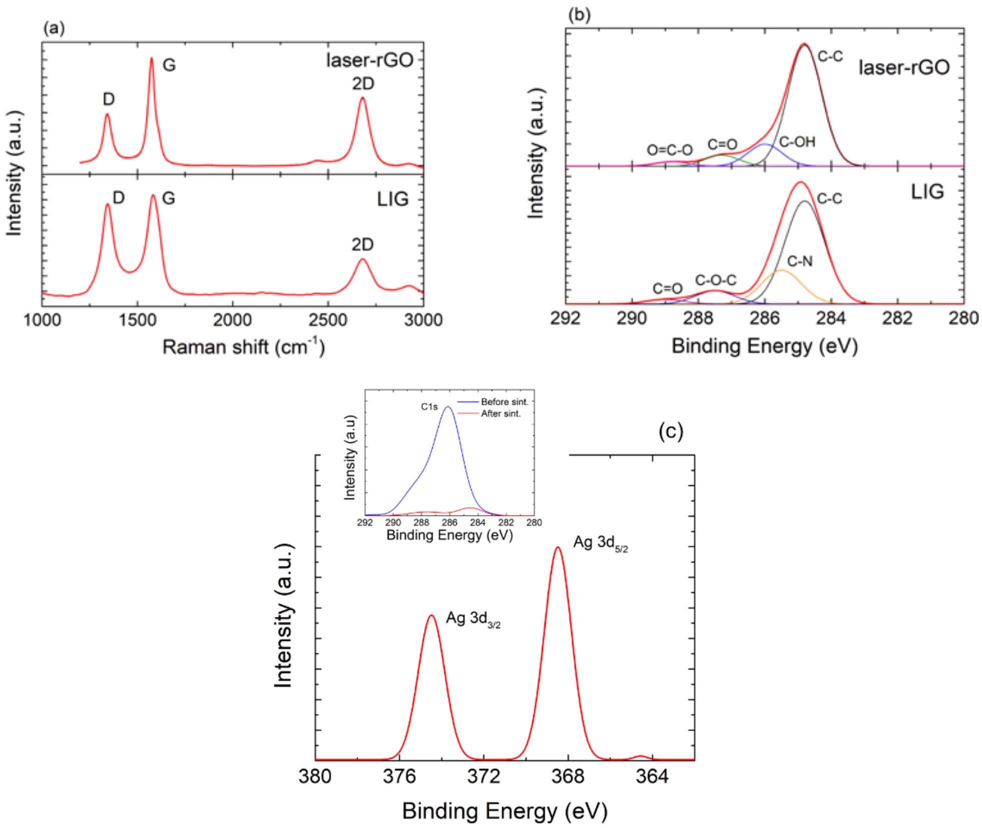


**Figure 4.** (a) Comparison of the Raman spectra obtained from the laser-rGO and LIG sheets. The laser power used to produce the samples was 100 mW at an excursion rate of 3 min cm$^{-2}$. (b) Comparison of the C1s peaks from the XPS spectrum of LIG and laser-rGO. The laser excursion rate was set to 3

min cm-2 for a laser power of 100 mW. (c) XPS spectrum of Ag 3d core level of Ag-ink patterns after drying and sintering steps. Inset shows a comparison of the C1s peaks before and after these steps.

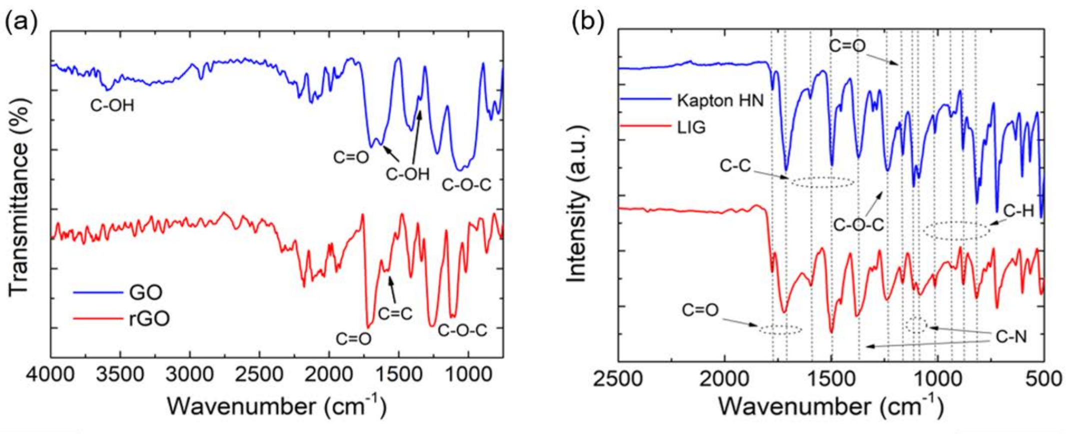


**Figure 5.** (a) ATR-FTIR spectroscopy of the GO before and after the reduction. (b) DRIFT spectra of the Kapton® polyimide before and after the laser irradiation. (number of scans: 1024, resolution 1 cm-1.

**Table 2.** Planar IDE capacitors: theoretical and experimental dimensions.

| Parameter | Model (mm) | Laser-rGO & LIG (mm) | Inkjet-printed (mm) |
|---|---|---|---|
| Fingers length (*l*) | 10 | 10.4 ± 0.5 | 9.8 ± 0.2 |
| Fingers width (*w*) | 1 | 1.32 ± 0.13 | 1.02 ± 0.05 |
| Fingers interspacing (*i*) | 0.5 | 0.55 ± 0.02 | 0.47 ± 0.04 |
| Electrodes separation (*s*) | 0.5 | 0.54 ± 0.02 | 0.51 ± 0.05 |

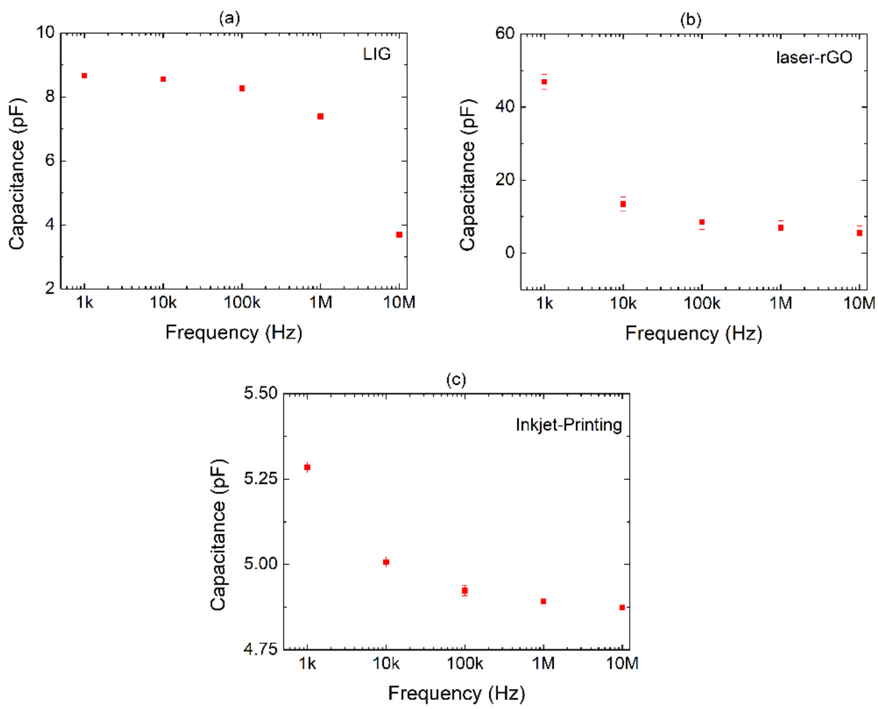


**Figure 6.** Capacitance as a function of the frequency at 70%RH, and a fixed temperature of 40 °C for the capacitors with LIG-based electrodes (a), laser-rGO-based electrodes (b) and inkjet-printed ones (c). Error bars according to the hysteresis loop due to the increase/decrease of RH are shown.

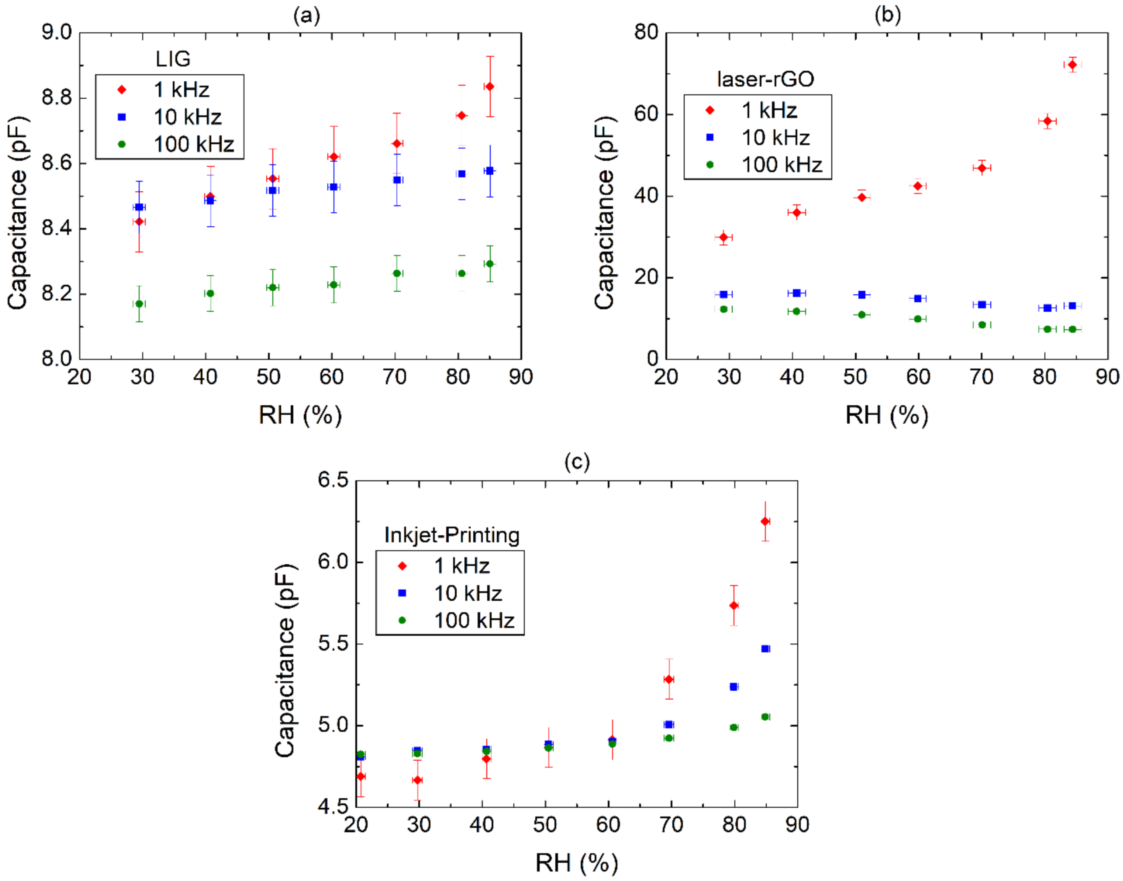


**Figure 7.** Response of the humidity sensors: capacitance as a function of the relative humidity, RH(%), for three frequencies at a fixed temperature of 40 °C. Error bars according to the hysteresis loop due to the increase/decrease of RH are shown.

**Table 3.** Comparison among the three different flexible capacitive humidity sensors.

| | LIG | Laser-rGO | Inkjet |
|---|---|---|---|
| Sensitivity (fF/%RH) | 7.44 at 1 kHz<br>2.00 at 10 kHz<br>2.20 at 100 kHz | 764 at 1 kHz<br>66.28 at 10 kHz<br>89.32 at 100 kHz | 24.71 at 1 kHz<br>10.28 at 10 kHz<br>3.57 at 100 kHz |
| Nonlinearity | 0.50% at 1 kHz<br>0.29% at 10 kHz<br>0.33 at 100 kHz | 4.81% at 1 kHz<br>4.76% 10 kHz<br>5.41% at 100 kHz | 7.07% at 1 kHz<br>1.43% at 10 kHz<br>1.04% at 100 kHz |
| Thermal drift (fF/°C) | < 1 at 1 kHz<br>5.88 at 10 kHz<br>4.47 at 100 kHz | 218.63 at 1 kHz<br>60.01 at 10 kHz<br>73.06 at 100 kHz | 17.20 at 1 kHz<br>23.81 at 10 kHz<br>26.24 at 100 kHz |
| Equivalent parallel resistance (MΩ) at 50%RH | 678 at 1 kHz<br>123 at 10 kHz<br>3.72 at 100 kHz | 0.100 at 1 kHz<br>0.097 at 10 kHz<br>0.086 at 100 kHz | 2100 at 1 kHz<br>385 at 10 kHz<br>110 at 100 kHz |

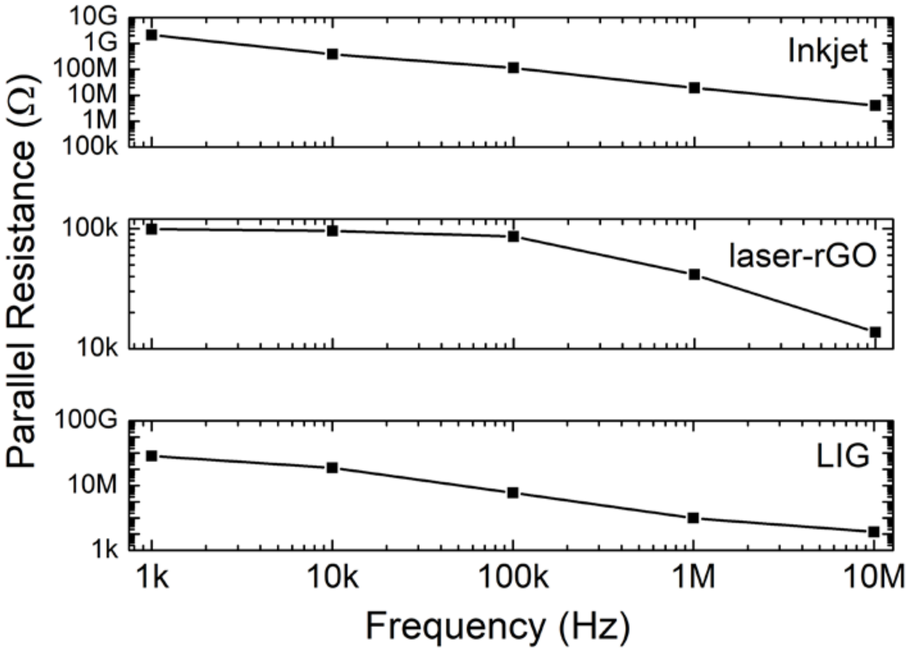


**Figure 8.** Equivalent parallel resistance, $R_p$, of the capacitive structures as a function of the frequency measured at the fixed conditions of 50%RH and 40 °C.

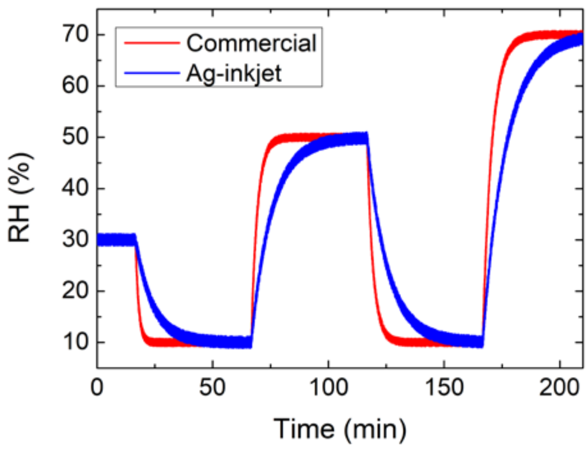


**Figure 9.** Transient response of the Ag-ink IDE capacitor.